Abstract.   Current methods employed by the United States Geological Survey (USGS) to measure river discharge are manpower-intensive, expensive, and during high flow events require field personnel to work in dangerous conditions. Indirect methods of estimating river discharge, which involve the use of extrapolated rating curves, can result in gross error during high flow conditions due to extrapolation error and/or bathymetric change. Our goal is to develop a remote method of monitoring volumetric discharge that reduces costs at the same or improved accuracy compared with current methods, while minimizing risk to field technicians. We report the results of Large-Scale Particle Image Velocimetry (LSPIV) and Acoustic Doppler Velocimetry (ADV) measurements conducted in a wide open-channel under a range of flow conditions, i.e. channel aspect ratio ($B/H = 6.6 - 31.9$), Reynolds number ($Re_H = 4,950 - 73,800$) and Froude number ($Fr = 0.04 - 0.46$). Experiments were carried out for two different channel cross-sections (rectangular and asymmetric-compound) and two bathymetric roughness conditions (smooth glass and rough gravel bed). The results show that the mean surface velocity normalized by the depth-averaged velocity (the velocity index) decreases with increasing δ^*/H, where δ^* is the boundary layer displacement thickness) and that the integral length scales, $L_{11,1}$ and $L_{22,1}$, calculated on the free-surface vary predictably with the local flow depth. Remote determination of local depth-averaged velocity and flow depth over a channel cross-section yields an estimate of volumetric discharge.

1. Introduction

Volumetric discharge (the integrated instantaneous volume flux across a specific cross-sectional area) is a fundamental hydrological parameter in the characterization of river and water conveyance channel dynamics. Its accurate measurement is essential for operating water distribution infrastructure, responding to drought and flood events, and predicting transport of sediment and environmental contaminants. River discharge data is used to forecast reservoir levels and to assess environmental regulations such as required freshwater discharges to estuaries. Accurate, robust, and inexpensive measurements of volumetric discharge are crucial to the sustainable use of water as a global resource; and is becoming increasingly important under anthropogenic climate change [Johnson and Cowen, 2014].

Measurements of volumetric discharge are conducted worldwide and are of global significance. Consider, for example, the techniques used by the United States Geological Survey (USGS), which typically involve dividing a river cross-section into many segments. In each segment concurrent measurements of the flow depth and of the streamwise velocity profile are made allowing local values of the depth-averaged velocity to be calculated. The total volumetric discharge is then calculated as,

$$Q = \sum_{i=1}^{N} \overline{U}_{Bi} B_i H_i \tag{1}$$

where Q is volumetric discharge $[m^3/s]$ and is equal to the summation of the product of each segment's depth-averaged velocity, $\overline{U}_{Bi}$ [m/s], times its area (equal to the product of the segment's width, B_i, and depth, H_i) [Rantz, 1982]. Given that velocity and bathymetry can vary strongly across a river's cross-section, accurate determination of discharge requires measurements in enough segments to accurately represent the river

cross-section ($i = 1, 2, ..., N$). Typically Acoustic Doppler Velocity Meters (ADVMs) or current meters, both electromagnetic or mechanical, are traversed crossed a river to make these measurements. Again, considering the example of the USGS, this direct method of measuring volumetric discharge is conducted several times a year at each of the approximately 7,300 gaging stations currently operated by the USGS, resulting in a process that is time consuming, expensive and potentially dangerous.

Rating curves, which express the empirical dependence of a river's discharge on its stage (the height of the river surface relative to a site-specific georeferenced datum), permit continuous estimates of river discharge through continuous measurements of stage. Because a river's stage is a simpler measurement to make, at most stream gaging stations this indirect method of estimating discharge is used between direct measurements. For rivers that have a stable cross-section and uniform flow conditions, this method is typically accurate to within 5% [Sauer and Meyer, 1992]. However, existing rating curves can rapidly be rendered obsolete if the cross-section of the river is highly dynamic (due to erosion or accretion, e.g., Figure 4 of Mason and Weiger [1995]). Extensive aquatic vegetation growth, debris accumulation, or other channel manipulation can also invalidate an existing rating curve.

While accurate discharge data would ideally be available for all flow conditions, the need is vital during extreme events. Volumetric flow rate is an essential boundary condition required by models used to issue flood warnings, evacuation notices and official statements about the potential for dangerous conditions. The issuance of prompt and accurate flood forecasts is essential to mitigate adverse economic impacts and the loss of human lives. Ideally government agencies would make near-real-time measurements of discharge and

stage during extreme events. However, this is not feasible with current technology as it requires the deployment of field teams during extreme conditions and the risks to human life and equipment are not acceptable.

Several research efforts have attempted to meet this near-real-time data need by leveraging remote sensing techniques. Significant efforts built around radar technology (e.g., the USGS task committee Hydro 21) focus on the ability of radar to measure surface water mean velocity [e.g., Costa et al., 2000; Lee et al., 2002a; Mason et al., 2002; Melcher et al., 2002; Lee et al., 2002b; Nicolas et al., 1997]. In general radar is found to be as accurate as traditional methods with some exceptions in the far-field. However, each of these studies required that an additional measurement system be used to assess the river's cross-sectional area to facilitate calculation of volumetric discharge. Further, much like ADVM measurements over larger distances, the instantaneous measurements are noisy and require significant averaging in time to develop an accurate estimate of the mean velocity field.

Quantitative imaging (QI) techniques [Sveen and Cowen, 2004] such as Large-Scale Particle Image Velocimetry (LSPIV) and Space-Time Image Velocimetry (STIV) have been the focus of several research efforts [e.g., Creutin et al., 2002; Weitbrecht et al., 2002; Fujita and Tsubaki, 2002; Creutin et al., 2003; Fujita et al., 1998]. One of the primary benefits of QI techniques is that they are capable of measuring accurate instantaneous velocity data in two dimensions at a wide range of spatial and temporal scales over the imaging device's field-of-view (FOV). This represents a capability previously unattainable by conventional stream gaging techniques. Despite this clear advantage, to determine the river cross-sectional area each of the above studies used a second system

(e.g., ground penetrating radar) that was traversed across the river to measure variation in local bathymetry.

The technique that is developed here further capitalizes on the strengths of QI techniques, specifically LSPIV, in the process of stream gaging and eliminates the need to traverse a second measurement system across the river to determine bathymetry. From the captured instantaneous velocity fields, local information regarding the depth-averaged velocity and bathymetry can be gleaned. Large-scale, energy-containing, coherent turbulent structures, which include the streamwise counter-rotating vortices, turbulent boils and all structures that connect the bed to the free surface, are ubiquitous in open channel flow and scale with the flow depth; thus enabling the proposed approach to discharge calculation.

The following sections present this novel approach. The proposed technique is calibrated and validated based on laboratory experiments carried out in a wide-open channel flume. The details of the experimental facilities and techniques are documented in the next section which is followed by the presentation of the experimental results. The paper concludes with a validation of the methodology developed herein.

2. Experimental Methods

2.1. Facility

Three sets of experiments were completed in a recirculating wide open-channel located in the DeFrees Hydraulics Laboratory at Cornell University (Figure 1). This facility has a test section that is 15 m in length, $B = 2$ m wide and can accommodate a maximum flow depth (H) of 0.64 m. The relatively large width of the test section makes it perfectly suited to the study of river flows as the aspect ratio (B/H) can be established such that

$B/H > 30$, consistent with those for natural rivers [Fischer et al., 1979]. The facility was built to study secondary flows and scale-dependent dispersion due to meandering motions [Liao and Cowen, 2002; 2010]. The flow is generated and sustained by two digitally controlled custom-built axial pumps that are located beneath the test section. The pumps drive the water into the inlet section through two PVC pipes, each 0.406 m in diameter. In the inlet section a 51 mm thick stainless steel grid with 0.10 m × 0.10 m square openings followed by 0.76 m thick honeycomb material with 6.4 mm circular openings, condition the flow and break down large flow structures that are created by the two supply pipes. The flow is further conditioned by a 4:1 contraction in the vertical prior to its arrival at the test section. A 3.2 mm diameter polycarbonate rod is located orthogonal to the flow on the bed at the entrance to the test section to trip the boundary layer. The test section bed and side-walls are constructed from 12.7 mm thick plate glass, allowing for excellent optical access. An adjustable weir is attached at the end of the test section to force the exiting flow to become critical thereby preventing surface disturbances from propagating upstream into the test section [Johnson, 2015].

The bed of the channel test section is horizontal. Liao and Cowen [2010] demonstrated through a scaling analysis that in the same facility with depth-averaged velocity, $U_B \sim 0.45$ m/s and flow depth, $H \sim 0.08$ m, acceleration was not important. As all of our flows are forced more mildly than the Liao and Cowen [2010] conditions (their $u^* > 20$ mm/s, while our $u^* < 20$ mm/s, see Tables 1-3, where u^* is the friction velocity) and are, in general, deeper and/or slower relative to Liao and Cowen [2010], the streamwise acceleration can be neglected in all of our tests as well.

All measurements reported herein were made approximately 8.9 m downstream from the beginning of the test section to allow sufficient distance for the flow to become fully developed. Two conditions are implied by the use of the term *fully-developed.* The first refers to when vertical profiles of streamwise velocity are normalized by the boundary layer thickness and maximum velocity and the normalized profiles become self-similar. The objective in setting measurement locations far downstream of the beginning of the test section is to ensure that vertical profiles are self-similar. Although the results are not shown here, all experimental cases were examined for self-similarity and each were found to be self-similar. The second condition implied by the term fully developed refers to whether or not the growing boundary layer reaches the free surface and in doing so, completely entrains the homogenous isotropic turbulence issuing from the grids in the inlet section (see Figure 1). As will be discussed in the next sections, the ratio formed by the displacement thickness normalized by the flow depth, δ^*/H ($\delta^* = \int_0^H (1 - U(z)/U_{max})\, dz$, where U_{max} is the local maximum velocity), systematically quantifies this situation. This subject is treated further in section 2.2.1.

The coordinate system used in this work has its origin located at the beginning of the test section, on the centerline of the channel at the bed [Johnson and Cowen, 2014]. The streamwise, transverse and vertical directions are given by x, y, and z coordinates, respectively.

2.2. Experimental Cases

With the objective of understanding turbulent surface features for an anticipated wide range of bathymetric conditions that are present in the field, three distinct

bed/bathymetric conditions were created and a total of twenty-six individual experiments were carried out and are documented herein.

2.2.1. Smooth Bed

To establish flow depth and Reynolds number dependencies for planar smooth bed conditions, sixteen experimental cases were run using the facility's rectangular smooth glass walls as the flow boundary condition. The flow depth, H, was varied from 0.06 - 0.31 m and the depth-averaged velocity, $U_b = \int_0^H U(z)/H \, dz$, ranged from 0.06 - 0.35 m/s (Table 1). Relevant dimensionless parameters characterizing each smooth bed experiment are listed in Table 1 and include the aspect ratio, B/H, and the displacement thickness normalized by the flow depth, δ^*/H, which is a measure of the boundary layer development. The aspect ratio spanned $B/H = 6.6 - 31.9$. Therefore, consistent with the criteria established by Nezu and Nakagawa [1993] (wide open-channels: $B/H > 5$, narrow open-channels: $B/H \leq 5 - 6$), each flow case presented here is properly classified as a wide open-channel flow and the surface features discussed herein are consistent with those observed in wide open-channels. As noted by Tamburrino and Gulliver [2007] and Albayrak and Lemmin [2011], the number of streamwise counter-rotating vortices in a wide open-channel is a function of the aspect ratio. These structures, and the resulting secondary flows they promote, have a marked influence on the free-surface turbulence characteristics and will be discussed in the next section.

In addition to counter-rotating vortices influencing the free surface, bottom-generated structures, such as turbulent boils and hairpin vortices, which originate from the boundary layer, also influence the free surface. Understanding how these turbulent surface features change with the developmental state of the boundary layer, characterized by δ^*/H, is of

great importance in this study. Figure 2a, which depicts normalized velocity profiles and the logarithmic law modeled extension to the bed (see Section 3.1.1), illustrates that larger values of the displacement thickness are the result of larger regions of slower flow relative to U_{max}. The ratio δ^*/H, therefore, provides physical insight into the link between the free-surface turbulence and the extent to which it is influenced by boundary layer turbulence. It is proportional to the fraction of the water column that is subsumed by the bottom boundary layer; the larger the ratio, the greater the extent that the free-surface turbulence is dominated by boundary layer turbulence. Its magnitude provides information on how strongly correlated the free-surface turbulent signatures are with bed-generated motions.

2.2.2. Compound Channel

To study effects associated with variable bathymetry and to mimic typical river cross-sections, both with and without flood plains, three experiments were carried out with a polyvinyl chloride (PVC) false-bottom section added to the channel (Figure 3a). The maximum height of the added PVC section is 0.16 m. The height of the section linearly decreases over an 0.80 m span, creating bathymetry that varies in the lateral but not the longitudinal direction (Figure 3b). Two experiments were conducted where the channel was filled above the maximum height of the added PVC section ($H = 0.20$ and 0.26 m), creating overbank flow conditions and a flood plain. One experiment was conducted at bank-full conditions ($H = 0.15$ m).

The key dimensionless parameter for the compound channel cases is the relative flow depth, $D_r = h/H$, where h represents the flow depth over the flood plain and H is the flow depth in the main channel (see Table 2). In these experiments D_r varied from $0-0.4$. Although not shown here, the strength of free-surface turbulent features increases with

decreasing relative flow depth, a trend that is consistent with other investigations [Prinos et al., 1985].

2.2.3. Gravel Bed

Lastly, to facilitate study of increased bed roughness on free-surface turbulence expression, a bed of loose gravel with median particle diameter, $D_{50} = 6.1$ mm, and root mean square bed roughness height, $k_{rms} = 21.6$ mm, was added to the channel. The root mean square bed roughness height, which is equal to the standard deviation of the gravel bed elevation above the channel's glass bed, was manually measured at 80 different locations within the gravel bed. The median particle diameter was assessed through passing the bed material through a series of sieves. The width of the gravel bed (~ 0.90 m) covered just under half of the channel width and ran from the beginning of the test section to well past the location where the measurements were made (12 m long strip), allowing sufficient distance for the resulting flow to develop fully. The gravel bed was leveled manually and no motion of the gravel was observed during any of these tests (highest Shield's parameter for rough bed cases, $\theta = \tau/(\rho_s - \rho)gD_{50} = 0.004$, where τ is the bed shear stress, g is the gravitational acceleration, and ρ and ρ_s are the density of water and the bed material, respectively). This observation was confirmed by examination of the images taken with the LSPIV system for each experimental case. An image of the gravel bed and subsequent FOV are shown in Figure 4.

For the rough bed cases, the key parameter is the ratio of the root mean square roughness height to the flow depth, k_{rms}/H. This parameter quantifies the fraction of the water column that is composed of the loose gravel. In our experiments, k_{rms}/H varies from $0.10 - 0.29$ (Table 3).

2.3. Large-scale PIV Measurements

To characterize the free surface of each experimental case listed in Tables 1-3, LSPIV was employed. PIV is a powerful and well-established fluid velocity measurement technique capable of instantaneous charactization of velocities in two or three dimensions [e.g., Cowen and Monismith, 1997]. The fundamental concept of PIV involves tracking the displacement of patterns of small passive particles between two images, separated by a finite time, Δt. In this manner instantaneous measurements of the velocity field over the FOV are obtained. By collecting several instantaneous measurements over a period of time, an ensemble-averaged mean velocity field can be determined. LSPIV, coined by Fujita et al. [1998], is an extension of traditional PIV, in which the instantaneous surface velocity field is measured in hydraulic flows of interest.

For the experiments reported herein the laboratory flow is seeded with small buoyant Pliolite VTAC-L particles. The particles have a specific gravity, $SG = \rho_p/\rho = 1.03$, where ρ_p is the particle density, and were sieved to a particle diameter (d_p) range of 0.42 - 0.60 mm. The particle Stokes number is small, $St = \tau_R/\tau_\eta$, where $\tau_R = \rho_p d_p^2/18\mu$ is the particle relaxation time (μ is the viscosity of water) and $\tau_\eta = \sqrt{\nu/\epsilon}$ is the Kolmogorov time scale (ν is the kinematic viscosity of water and ϵ is turbulence dissipation), with typical value of $St = 0.092$, confirming that the particles are passive tracers.

The approximate FOV, 1.93 x 2.03 m in the streamwise and transverse directions, respectively, was imaged with a 12-bit per pixel IMPERX IGV-B2020 CCD camera (2060 $\times$ 2056 pixel array) fitted with a 20 mm, $f/2.8$ Nikon Nikkor lens [Johnson and Cowen, 2014]. The camera was mounted $\sim$ 3 m above the channel bed. The spatial resolution of the camera, which was determined by analyzing images of a checkered calibration target

at the height of the free-surface, ranges from 1.01-1.08 mm/pixel and is a function of flow depth.

Mathworks MATLAB was used to control image integration duration and to establish the elapse time between images constituting a pair, $\Delta t = 75 - 400$ ms. The goal in selecting an appropriate Δt, which varied with the mean flow speed for each experiment, was to allow sufficient time for particles to translate in both the streamwise and lateral directions while not translating so far as to decorrelate the particle tracer patterns within an image pair [Cowen and Monismith, 1997]. The camera integration time was held constant at 3.00 ms, which provided a balance between allowing sufficient time to develop good dynamic range in the images without allowing particle image streaks. Approximately 4000 image pairs were captured at 1 Hz for each experimental condition (temporal record length greater than 60 minutes). The IMPERX BobCat GEV software was used to stream the images to an external solid-state hard drive over an eSATA bus in real-time. Eight 500 W halogen lamps mounted above the flume provided a constant white light source (four equispaced in the lateral direction on the upstream and downstream sides of the FOV).

To remove the stationary image background, the raw images were pre-processed by subtracting one image within an image pair from the other [Honkanen and Nobach, 2005; Mejia-Alvarez and Christensen, 2013]. This technique removes the background completely while preserving the particle images as their location changes over the image pair. This technique was particularly useful in the analysis of the gravel bed images, where the gravel bed created a background that varied significantly in brightness intensity.

The pre-processed images were analyzed using the cross-correlation algorithm of Cowen and Monismith [1997] which was extended to be second-order accurate in space [Wereley and Meinhart, 2001] and implemented in a suite of FORTRAN codes (analysis details can be found in Johnson [2015]). The algorithm determines the minimum background intensity for each pixel across the entire image set. This minimum background is removed from images to enhance the signal-to-noise ratio of the images. Sub-window size was set at 64 × 32 pixels (approximately 0.06 m x 0.03 m in the streamwise and transverse directions, respectively). Results are post-processed with an adaptive Gaussian window filter [Cowen and Monismith, 1997] followed by a local median filter [Westerweel, 1994] to remove spurious velocity vectors. Typically 4%-11% of vectors are removed as spurious. Removed vectors are replaced using a Delaunay triangulation interpolation method. Finally, mean and turbulence velocity metrics are found through Reynolds decomposition, namely $U(t) = \overline{U} + u'(t)$, here U represents any velocity component, $\overline{U}$ is the temporal average, and $u'(t)$ is the instantaneous turbulence fluctuation.

2.4. ADV Measurements

In order to relate the free-surface flow field to the volumetric discharge it is necessary to compare the surface velocity to the depth-averaged velocity. All water column velocity measurements were collected by three-component Acoustic Doppler Velocimeters (ADV – Nortek Vectrino equipped with + firmware). The measurement volume is cylindrical with a fixed 6 mm diameter and a user adjustable length set to 8 mm for all measurements reported herein. Each point measurement was sampled for five minutes at 200 Hz. This record length was deemed sufficient to achieve convergence of the mean velocity to well within ±5% as verified by the bootstrap method [Efron and Tibshirani, 1993].

Vertical profiles of velocity were collected at the streamwise midpoint of the LSPIV image FOV ($x = 9.89$ m). For the smooth glass bed experiments, profiles were measured at the channel centerline ($y/B = 0$). For the gravel bed cases, they were made at the channel centerline, over the centerline of the gravel strip ($y/B = 0.23$) and over the centerline of the smooth glass bed ($y/B = -0.25$). For the compound channel cases, profiles were measured in the center of the main channel ($y/B = -0.35$), and when the flow depth permitted, measurements were made in two locations over the variable bathymetry between the main channel and flood plain ($y/B = \pm 0.08$) and in one location over the floodplain ($y/B = 0.35$) (see Figure 3b).

2.5. Ultrasonic Flowmeter

In order to validate the LSPIV approach to discharge measurement, concurrent independent measurements of volumetric discharge were collected with an ultrasonic flowmeter (FLUXUS ADM 7407). Transducers were mounted on both supply pipes. Discharge was determined by dividing the total volume of fluid flowing through both pipes over the course of the experiment by the total sampling time. Flowmeter accuracy ($\pm 3\%$) was verified by maintaining quality indicators in accordance with manufacturer recommendations - high signal quality values (≥ 8), high signal-to-noise ratio (≥ 3) and accurate reported values of the speed of sound in water.

2.6. Flow Depth Measurement

Flow depth was measured using two Banner S18UUAQ acoustic proximity sensors to detect the free-surface position. The sensors were placed immediately upstream of the LSPIV image FOV ($x = 7.23$ m) and were sampled at 200 Hz for the duration of each

test. The data were collected using Data Translation's EconSeries DT9813 USB data acquisition module.

3. Results

Calculation of volumetric discharge requires coincident measurements of local depth-averaged velocity and flow depth over a cross section (Equation 1). The local depth-averaged velocity is determined from the mean surface velocity field using the index velocity [Rantz, 1982] approach. Local flow depth is determined from a surface integral length scale used in conjunction with an empirical correlation with flow depth developed herein. The approach is developed and results are presented for the smooth bed experimental cases first and then tested for the compound channel experiments. The approach is then extended to include the effects of bed roughness. Finally, the overall technique is validated by comparing the volumetric discharge estimated from the remotely sensed images with the simultaneous and independent ultrasonic flowmeter measurements.

3.1. Smooth Bed

3.1.1. Depth-Averaged Velocity

To relate the surface velocities measured by the LSPIV system to depth-averaged velocities, the index velocity, $k = U_b/U_{\mathrm{surf}}$, where U_{surf} is the mean streamwise surface velocity, was determined for each experimental case. Because the ADV geometry prevents measurement of the near-bed region, to calculate depth-averaged velocities the measured full-depth profiles are extrapolated to the bed, using the log-wake law (as seen in Figure 2). Here, and in other studies of smooth bed open channel flow, when full-depth profiles of streamwise velocity are normalized by the inner wall variables, namely the friction

velocity, u^*, and the kinematic viscosity, ν, they follow the log-wake law given by,

$$\frac{U}{u^*} = \frac{1}{\kappa} \ln\left(\frac{zu^*}{\nu}\right) + A + \frac{2\Pi}{\kappa} \sin^2\left(\frac{\pi}{2}\frac{z}{H}\right) \qquad (2)$$

where κ is the von Kármán constant, A is the integration constant and the last term on the right is the wake function (Π is Coles wake parameter) [Kirkgöz, 1989]. To fit the smooth bed data to the logarithmic profile given in equation 2, the friction velocity for each experimental case was estimated via linear extrapolation of the Reynolds stress $(-\overline{u'w'})$ plot to the bed. This estimate was refined through fitting the total stress $(\tau/\rho = \nu dU/dz - \overline{u'w'})$ to a linear distribution $(\tau/\rho = u^{*2}(1 - z/H))$ in a least-squares sense. The integration and von Kármán constants were then determined in a least-squares sense by fitting the velocity profile to the log-wake law in a manner similar to Nezu and Rodi [1986].

For the smooth bed cases the von Kármán constant is given by $\kappa = 0.41$ and the wake strength parameter is found to be small, $\Pi = 0 - 0.1$. These values are consistent with the results of other investigations [Nezu and Rodi, 1986; Cardoso et al.,1989]. The value of the integration constant $(A = 2 - 5.3)$ varies somewhat across all the cases. This variation is also consistent with the results from other investigations (Cardoso et al. [1989], $A = 3.91 - 6.7$; Nezu and Rodi [1986], $A = 5.29 \pm 0.47$) and is attributed to the presence of secondary flows within the channel [Johnson, 2015].

The log-law extrapolated full-depth profiles are integrated numerically to yield depth-averaged velocity, U_b, and the index velocity, specific to each experimental case is calculated. The range of values for the smooth bed case reported in Figure 5, $k = 0.82 - 0.93$, is consistent with other investigations [Rantz, 1982; Harpold et al., 2006]. Knowledge of the velocity index permits the conversion of surface velocities to depth-averaged velocities.

Note that the variation observed in the velocity index is well correlated with the displacement thickness normalized by the flow depth. Despite the fact that displacement thickness is rarely used in the open channel flow community, we achieved a better correlation with the displacement thickness normalized by the flow depth as opposed to the boundary layer thickness normalized by the flow depth (Figure 3, Johnson and Cowen [2014]). We find this to be especially true for the shallowest flow cases where it becomes increasingly difficult to define where the boundary layer ends. The displacement thickness removes the ambiguity associated with determining where the boundary layer terminates and provides a physically based rationale for the variation observed in the index velocity.

3.1.2. Local Flow Depth Determination

To remotely determine the local flow depth, we exploit the presence of large-scale coherent structures, in general, and streamwise elongated vortices in shallow open channel flows, in particular. These structures are well documented in numerous investigations [Nezu, 1993; Shvidchenko and Pender, 2001] and their characteristic length scales consistently scale with the flow depth. Figure 6, which depicts two instantaneous surface streamwise velocity fields measured by our LSPIV system, proves the existence of these structures in our channel ($H = 0.63$ m, $U_B = 0.26$ m/s and $H = 0.20$ m, $U_B = 0.25$ m/s). The longitudinal streaks shown in Figure 6 are alternating bands of high momentum (red) and low momentum (yellow-green) fluid that are indicative of secondary flows influencing the free surface [Johnson and Cowen, 2014]. Tamburrino and Gulliver [1999] suggest that the number of counter-rotating vortices that cause these longitudinal streaks should increase with the aspect ratio of the flow and this trend is clearly observed in Figure 6.

To systematically quantify the size of these surface signatures, the integral length scale is calculated from the instantaneous turbulent velocity field. The integral length scale is the integral of the normalized spatial autocorrelation function of the turbulent velocity fluctuations shown below in equation 3,

$$L_{ij,k} = \int a_{ij,k}(r)dr \quad \text{where,} \quad a_{ij,k}(r) = \frac{\overline{u_i'\left(x_c - \frac{1}{2}r_k\right)u_j'\left(x_c + \frac{1}{2}r_k\right)}}{\sqrt{\overline{u_i'\left(x_c - \frac{1}{2}r_k\right)^2}\,\overline{u_j'\left(x_c + \frac{1}{2}r_k\right)^2}}} \quad (3)$$

where, $a_{ij,k}$ is the normalized spatial autocorrelation function, r is the spatial separation vector, and the overbar indicates temporal averaging [Johnson and Cowen, 2014; Variano and Cowen, 2008]. To calculate the integral length scale, a central difference approach was used and x_c indicates the x coordinate about which the correlation is performed. The integral length scale can be calculated using either streamwise ($i, j = 1$ direction) or transverse ($i, j = 2$ direction) velocity fluctuations and correlations can be determined in either direction ($k = 1$ or 2 indicating streamwise or transverse direction, respectively). Given that the bathymetry of rivers varies strongly in the transverse direction, only correlations performed in the streamwise direction lead to unambiguous determination of the lateral variation in bathymetry [Johnson and Cowen, 2014].

$L_{11,1}$ captures the characteristic streamwise length scale of the surface turbulence structures from the streamwise velocity fluctuations. Figure 7a shows the measured $L_{11,1}$ for the $U_B \approx 0.24$ and 0.34 m/s flow cases for each flow depth. With the exception of the deepest flow case ($H = 0.30$ m), it is clear that $L_{11,1}$ scales with H and depends weakly on Reynolds number. The $H = 0.30$ m flow case has a small value of $\delta^*/H = 0.07$, which indicates that the turbulent boundary layer is not sufficiently developed and that the surface turbulence signatures are dominated by decaying grid generated turbulence created in the inlet (Figure 1). Neglecting the side-wall region (which is influenced by

corner vortices), an average is taken across the center of the channel ($|y/B| \leq 0.3$) and is plotted in Figure 8a. Again, the strong correlation of $L_{11,1}$ with H is apparent ($R^2 = 0.95$) and we observe that $L_{11,1}/H \sim 2.8$.

$L_{22,1}$ captures the characteristic streamwise length scale of the surface turbulence structures using the transverse velocity fluctuation field. $L_{22,1}$, shown in Figures 7b and 8b, also correlates strongly with the flow depth ($R^2 = 0.96$) and is equal to approximately half the flow depth, $L_{22,1}/H \sim 0.5$. There is no indication of a consistent dependence on Reynolds number.

Given that the length scales of the surface turbulence scale with flow depth, it is anticipated that they will be much larger in natural rivers. The camera's FOV will ultimately dictate if there is sufficient streamwise spatial extent to accurately measure $L_{11,1}$, which requires approximately six times the spatial coverage to measure at the same accuracy as $L_{22,1}$. For this reason, we suggest $L_{22,1}$ as the preferred integral length scale for predicting flow depth and estimating volumetric discharge. Local flow depth then is determined by inverting the expression relating flow depth and $L_{22,1}$, given in Figure 8b, solving for flow depth and then substituting in local surface values of $L_{22,1}$.

3.2. Compound Channel

In order to study the effects of laterally changing bathymetry on the surface integral length scales the channel was fitted with the previously described false bottom, creating an asymmetric compound channel. It has been documented in numerous smooth and rough bed studies that the counter-rotating vortices that occur in shallow open channel flow, scale with the flow depth. By comparison, there have been fewer studies of counter-rotating vortices over variable bathymetry. To our knowledge, this is the

first study to examine the influence of these structures on the free-surface over variable bathymetry. A clear relationship between the integral length scale and flow depth over changing bathymetry lends further credence to the methodology developed in this investigation.

3.2.1. Depth-Averaged Velocity

Depth-averaged velocity was calculated for each compound channel flow case at up to three locations in the channel ($y/B = \pm 0.08$ and 0.35) provided that the flow depth was sufficient for measurement with an ADV. The index velocities were found to be the same as those determined for the smooth bed cases for similar flow depths and flow speeds and the results are omitted here.

3.2.2. Local Flow Depth Determination

$L_{11,1}$ for the three compound channel cases is plotted in Figure 9b along with the cross-section of the channel bathymetry (Figure 9a). The floodplain spans $y/B = 0.20 - 0.50$, the linearly sloping bathymetry extends from $y/B = -0.20$ to 0.20 and the main channel covers $y/B = -0.20$ to -0.50. It is readily apparent that $L_{11,1}$ is greater over the main channel than over the flood plain for the overbank flow cases. There is also a gradual transition that occurs between $y/B = -0.20$ to 0.20, which is evidence of the integral length scale adjusting to the change in flow depth introduced by the sloping bathymetry. In terms of using the integral length scale to predict flow depth, these results are quite encouraging.

For the $H = 0.20$ m case, the magnitude of $L_{11,1}$ is comparable to the measured smooth bed values at similar flow depths. For the deeper $H = 0.26$ m case, $L_{11,1}$ over the flood plain is also in good agreement with the corresponding smooth bed case, however,

over the main channel, values of $L_{11,1}$ are lower than expected which is attributed to an insufficiently developed boundary layer. Comparing δ^*/H over the main channel ($\delta^*/H = 0.05$) with the deepest smooth bed case at a similar depth-averaged velocity ($H = 0.31$, $U_b = 0.24$, $\delta^*/H = 0.07$) confirms this conclusion.

The behavior of $L_{22,1}$ exhibits the same trend as $L_{11,1}$ with larger values over the main channel and decreasing values over the variable bathymetry and the flood plain (Figure 9c). The $H = 0.20$ m flow case shows evidence of a shallow mixing layer developing at $y/B = 0 - 0.1$, where values of $L_{22,1}$ go to zero. For the $H = 0.15$ and 0.20 m flow cases the agreement with the values of $L_{22,1}$ for smooth bed cases at similar flow depths is good. For the $H = 0.26$ m case, the value of $L_{22,1}$ over the flood plain is in good agreement with the smooth bed cases but are somewhat lower than expected over the main channel due to the insufficiently developed boundary layer. The general consistency in the magnitude of $L_{11,1}$ and $L_{22,1}$ between the smooth bed and compound channel flow cases allows the flow depth for the compound channel cases to be estimated using the expressions given in Figure 8.

3.3. Rough Gravel Bed

It has been well documented that bed roughness affects wall-bounded flows by altering the mean streamwise velocity profiles in the wall region [e.g., Krogstad et al., 1992]. Moreover, the addition of roughness enhances the vertical velocity fluctuations significantly across much of the boundary layer and for all wavenumbers (see Figure 12 in Krogstad et al., [1992]). It has also been demonstrated that bed roughness enhances and stabilizes the presence of secondary flows in wide-open channels [Albayrak and Lemmin, 2011; Nezu, 2005]. It is anticipated, and confirmed in this section, that roughness decreases the index

velocity. Further, in light of the redistribution of the vertical velocity fluctuations into surface parallel component directions due to the kinematic boundary condition in the vicinity of the free-surface [McKenna and McGillis, 2004; Cowen et al., 1995], we were also interested in studying the effect that enhanced vertical velocity fluctuations might have on the surface integral length scales.

3.3.1. Depth-Averaged Velocity

For each rough bed case, full-depth profiles of streamwise velocity were measured over the centerline of the gravel strip ($y/B = 0.30$), over the centerline of the smooth bed ($y/B = -0.25$) and on the channel centerline ($y/B = 0$). Representative profiles at each location were shown previously in Figure 2a, where it is clear that the presence of the bed roughness affects the velocity throughout the entire water column. This effect is not confined to the immediate vicinity of the roughness as demonstrated by the velocity profile measured on the channel centerline ($y/B = 0$), which is ~ 0.10 m from the edge of the bed roughness strip. The shallower profile over the roughness has a smaller value of depth-averaged velocity and the index velocity is likewise smaller as demonstrated by the hollow markers shown in Figure 5, $k = 0.69 - 0.92$. Note the trend of decreasing index velocity with increasing δ^*/H is consistent for both the smooth and rough bed cases in Figure 5.

3.3.2. Local Flow Depth Determination

As demonstrated in section 3.1.2, the integral length scales, both $L_{11,1}$ and $L_{22,1}$ scale with the flow depth. Figure 10a depicts $L_{11,1}$ computed for the rough bed cases and here again it scales with H. It is also observed that relative to the smooth bed section $L_{11,1}$ decreases over the rough bed, which is located between $y/B = 0.05 - 0.5$. This suggests

that the presence of the gravel bed ($k_{rms} = 2.16$ mm) constitutes a change in flow depth for the shallowest cases, $H = 0.08 - 0.15$ m, where $k_{rms}/H = 0.14 - 0.29$. When $L_{11,1}$ is averaged over the central core of the flow, its dependence on flow depth is revealed (Figure 11a). It is evident in Figure 11a that the slope of the expression for the rough bed cases ($m = 2.45$) relating flow depth to $L_{11,1}$ is quite close to the smooth bed slope ($m = 2.79$), which is also depicted. The underdevelopment of the boundary layer relative to the flow depth for the deepest flow cases ($H = 0.20$ m, $U_B = 0.04 - 0.22$ m/s) is also evident.

The transverse integral length scale, $L_{22,1}$, for the rough bed cases exhibits the same dependence on flow depth (Figure 10b) and here again the correlation with flow depth is stronger (Figure 11b). For the shallowest case ($H = 0.07$ m), $L_{22,1}$ becomes negative in the transition from the smooth and rough bed (Figure 10b). This behavior is characteristic of a shallow mixing layer in which large scale eddies are generated at the interface between two flows of different characteristic velocities [Uijttewaal and Booij, 2000]. This region is neglected in the averaging of the data used to generate Figure 11b.

The expressions that relate $L_{22,1}$ to H for both the smooth bed and rough bed cases are shown in Figure 11a and Figure 11b. The slopes of these expressions are quite close. The minor differences are attributed to experimental uncertainty and confinement effects resulting from the addition of a mixing layer in the center of the channel which reduces the lateral extent of the counter-rotating vortices. The expression given in Figure 11b is inverted to solve for the local flow depth for the rough bed cases.

3.4. Volumetric Discharge Determination

Thus far we have demonstrated that the velocity index decreases with the increasing ratio of displacement thickness to flow depth. We have also demonstrated that for a

variety of different bathymetric conditions, the integral length scale, $L_{22,1}$, scales with the local flow depth. Knowledge of these two variables over a given cross-section enables calculation of volumetric discharge.

For the experimental cases presented above the mean surface velocity profiles captured by the LSPIV system are converted to profiles of depth-averaged velocity using the index velocity that are specific to each flow case. The flow depth is determined by using surface values of $L_{22,1}$ together with the linear relations presented in Figures 8b and 11b. LSPIV estimates of volumetric discharge are compared with the independent measurements of volumetric discharge from the ultrasonic flowmeter. As observed in Figure 12, with the exception of two experimental cases ($Q_{LSPIV} = 468.7$ and 582.1 m^3/h), the agreement between the measured and estimated discharge is excellent. The two cases which do not agree with measurements from the flowmeter are both deep cases where the boundary layer is not fully developed (smooth bed: $H = 0.30$ m, $\delta^*/H = 0.07$ and rough bed, $H = 0.20$ m, $\delta^*/H = 0.23$).

4. Conclusion

We present the development of an LSPIV-based approach to remotely determine volumetric discharge from free surface imagery. In a series of experiments that spans three bed roughness and bathymetric conditions we demonstrate that the surface velocity together with the velocity index can be used to predict lateral profiles of depth-averaged velocity. We further, demonstrate that the integral length scale, which is determined from the same remotely sensed images used to calculate depth-averaged flow, is a powerful and reliable predictor of local flow depth. Our preferred integral length scale in the calculation of volumetric discharge is $L_{22,1}$, as it has better spatial convergence characteristics

relative to $L_{11,1}$, allowing a smaller overall FOV to be imaged. Using this methodology, excellent agreement between predicted and measured volumetric discharge is achieved for the majority of the experimental flow cases. The method used here to remotely measure volumetric discharge provides a new and considerably safer and lower cost method of monitoring river discharge, particularly during extreme events.

One in situ requirement that still exists in our approaching to using LSPIV to remotely determine volumetric discharge results from the conversion of surface velocities to depth-averaged velocities using the index velocity. As in our work, investigators previously have directly measured vertical profiles of velocity to accurately assess the index velocity [Le Coz et al., 2010; Polatel, 2006; Dramais et al., 2011; Gunawan et al., 2012; Harpold et al., 2006; Sun et al., 2010]. Other investigations use the USGS standard value for the velocity index, k=0.85 [Costa et al., 2000; Creutin, 2003; Melcher et al., 2002]. Given that we have demonstrated that the velocity index varies with displacement thickness (Figure 5), which varies with Reynolds number, bed roughness, and bathymetry in our study, the use of a singular, laboratory-determined velocity index over a channel cross-section provides a valid estimate but not an accurate result. Indeed, Dramais et al., [2011] and Le Coz et al., [2010] suggest that the use of the standard USGS value of k=0.85 might be the largest source of error in volumetric discharge predictions. Our research in developing remote methods of determining the velocity index is on going.

Future research efforts should focus on how widely the correlations determined in this investigation ($L_{11,1}2.79H$ and $L_{22,1}0.52H$) vary for different field sites and how the dynamics of large-scale coherent structures contribute to the variation observed in their measurements. We believe the methodology that we have developed here will be applica-

ble to a large number of field sites. However, special considerations will be required for implementation in field sites that are affected by vegetation or stratification, as these conditions will limit the growth of depth-scale coherent structures (e.g., King et al., [2012]). Lastly, we anticipate that this methodology can be readily implemented from a number of different platforms including unmanned aerial vehicles and thermal infrared imagery.

References

Albayrak, I., and U. Lemmin (2011), Secondary currents and corresponding surface velocity patterns in a turbulent open-channel flow over a rough bed, *J. Hydr. Eng., 137*(11), 1318–1334.

Cardoso, A. H., W. H.Graf, and G. Gust, G, (1989), Uniform flow in a smooth open channel. *J. of Hydr. Rese., 27*(5): 603-616.

Cowen, E. A. and S. G. Monismith (1997), A hybrid digital particle tracking velocimetry technique, *Exp. in Fluids, 22*(3): 199-211.

Cowen, E. A., S. G. Monismith, and J. R. Koseff (1995), Digital particle tracking velocimetry measurements very near a free-surface, *Air-Water Gas Transfer*, 135-144.

Creutin, J. D., M. Muste, A. A. Bradley, S. C. Kim, and A. Kruger (2003), River gaging using PIV techniques: a proof-of-concept experiment on the Iowa River, *J. of Hydrology, 277*(3-4): 182-194.

Creutin, J. D., M. Muste, and Z. Li (2002), Traceless quantitative imaging alternatives for free-surface measurements in natural streams, *ASCE Conf. Proc*: Proceedings of Hydraulic Measurements and Experimental Methods.

Costa, J. E., K. R. Spicer, R. T. Cheng, F. P. Haeni, N. B. Melcher, E. M. Thurman, W. J. Plant, and W. C. Keller (2000), Measuring stream discharge by non-contact methods: A proof-of-concept, *Exp. Geophys. Res. Let., 27*(4): 553-556.

Dramais, G., J. Le Coz, B. Camenen, and A. Hauet (2011). Advantages of a mobile LSPIV method for measuring flood discharges and improving stage?discharge curves. *J. of Hydro-Environment Research*: 5(4), 301-312.

Efron, B., and R. J. Tibshirani, (1994) An introduction to the bootstrap. (Vol. 57). CRC press.

Fischer, H.B., E.J. List, R.C.Y. Koh, J. Imberger and N.A. Brooks (1979), Mixing in inland and coastal waters. Academic Press, New York.

Fujita, I., M. Muste, A. Kruger (1998), Large-scale particle image velocimetry for flow analysis in hydraulic engineering applications, *J. of Hydr. Res., 36*(3): 397-414.

Fujita, I. and R. Tsubaki (2002), A novel free-surface velocity measurement method using spatio-temporal images, *Proc. of Hydr. Measurements and Experimental Methods Conference.*

Gunawan, B., X. Sun, M. Sterling, K. Shiono, R. Tsubaki, P. Rameshwaran, and I. Fujita (2012). The application of LS-PIV to a small irregular river for inbank and overbank

flows. *Flow Measurement and Instrumentation*: 24, 1-12.

Harpold, A. A., S. Mostaghimi, P. P. Vlachos, K. Brannan, and T. Dillaha (2006), Stream discharge measurement using a large-scale particle image velocimetry (LSPIV) prototype, *Trans. ASABE, 49*(6): 1791-1805.

Honkanen, M., and H. Nobach (2005), Background extraction from double-frame PIV images, *Exp. in fluids, 39*(3): 348-362.

Johnson, E. (2015), The remote monitoring of surface velocity, bathymetry and discharge in rivers and open channel flows, Ph.D. dissertation, Cornell University, Ithaca, NY.

Johnson, E. and E. A. Cowen (2014), The remote monitoring of surface velocity, bathymetry and discharge in rivers and open channel flows, In *River Flow 2014* (No. EPFL-CONF-205197). Crc Press-Taylor and Francis Group.

A.T. King, R. O. Tinoco, E. A. Cowen (2012). A k?? turbulence model based on the scales of vertical shear and stem wakes valid for emergent and submerged vegetated flows. *J. of Fluid Mechanics 701*, 1-39

Kirkgöz, M. S. (1989), Turbulent velocity profiles for smooth and rough open channel flow, *J. of Hyd. Eng., 115*(11), 1543-1561.

Krogstad, P. Å., R. A. Antonia, and L. W. B. Browne, (1992), Comparison between rough-and smooth-wall turbulent boundary layers. *J. of Fluid Mech., 245*: 599-617.

Le Coz, J., A. Hauet, G. Pierrefeu, G. Dramais, and B. Camenen (2010). Performance of image-based velocimetry (LSPIV) applied to flash-flood discharge measurements in Mediterranean rivers. *J. of Hydrology*: 394(1), 42-52.

Lee, M.C., C. J. Lai, J. M. Leu, W. J. Plant, W. C. Keller, and K. Hayes (2002a), Non-contact flood discharge measurements using an X-band pulse radar (I) theory, *Flow*

Measurements and Instruments, 13(5): 265-270.

Lee, M.C., J. M. Leu, C. J. Lai, W. J. Plant, W. C. Keller, and K. Hayes (2002b), Non-contact flood discharge measurements using an X-band pulse radar (II) improvements and applications, *Flow Measurements and Instruments, 13*(5): 271-276.

Liao, Q. and E. A. Cowen (2002), The information content of a scalar plume – A plume tracing perspective, *Env. Fluid Mech., 2*(1-2): 9-34.

Liao, Q. and E. A. Cowen (2010), Relative dispersion of a scalar plume in a turbulent boundary layer, *J. of Fluid Mech., 661*: 412-445.

Mason, R. R., J. E. Costa, R. T. Cheng, K. R. Spicer, F. P. Haeni, N. B. Melcher, W. J. Plant, W. C. Keller, and K. Hayes (2002), A proposed radar-based streamflow measurement system for the San Joaquin river at Vernalis, California, *Proceedings of Hydraulic Measurements and Experimental Methods Conference*, ASCE Conf. Proc.

Mason, R. R., and B. A. Weiger (1995), Steam gaging and flood forecasting, A partnership of the U.S. Geological Survey and the National Weather Service: U.S. Geological Survey Fact Sheet FS-209-95.

McKenna, S. P., and W. R. McGillis (2004), The role of free-surface turbulence and surfactants in air-water gas transfer, *Int. J. of Heat and Mass Transfer, 47*(3), 539-553.

Mejia-Alvarez, R., and K. T. Christensen (2013), Robust suppression of background reflections in PIV images, *Meas. Sci. and Tech., 24*(2): 027003.

Melcher, N. B., J. E. Costa, F. P. Haeni, R. T. Cheng, E. M. Thurman, M. Buursink, K. R. Spicer, E. Hayes, W. J. Plant, W. C. Keller, and K. Hayes (2002), River discharge measurements by using helicopter-mounted radar, *Geo. Res. Let., 29*(22): 41-1.

Nicolas, K. R., W. T. Lidenmuth, C. S. Weller, and D. G. Anthony (1997), Radar imaging
of water surface flow fields, *Exp. in Fluids, 23*: 14-19.

Nezu, I., (2005), Open-channel flow turbulence and its research prospect in the 21st
century. *J. of Hydr. Eng., 131*(4): 229-246.

Nezu, I. and H. Nakagawa (1993), Turbulence in open channel flows. AA Balkema, Rot-
terdam.

Nezu, I., and W. Rodi (1986), Open-channel flow measurements with a laser Doppler
anemometer. *J. of Hydr. Eng., 112*(5): 335-355.

Polatel, C. (2006). Large-scale roughness effect on free-surface and bulk flow characteristics
in open-channel flows. ProQuest.

Prinos, P., R. Townsend, and S. Tavoularis (1985), Structure of turbulence in compound
channel flows. *J. of Hyd. Eng., 111*(9), 1246-1261.

Rantz, S. E. 1982. Measurement and Computation of Stream-flow: Vol. 1 Measurement
of Stage and Discharge, U.S. Geological Survey Water-Supply Paper. 2175.

Sauer, V. B., and R. W. Meyer (1992), Determination of error in individual discharge
measurements, U. S. Department of the Interior, U. S. Geological Survey.

Shvidchenko, A., and G. Pender (2001), Macroturbulent structure of open-channel flow
over gravel beds, *Water Resources Research, 37*(3): 709-719.

Sun, X., K. Shiono, J. H. Chandler, P. Rameshwaran, R. H. J. Sellin, and I. Fujita (2010).
Discharge estimation in small irregular river using LSPIV. *Proceedings of the ICE-Water
Management, 163*(5), 247-254.

Sveen, J. K., and E. A. Cowen, (2004), Quantitative imaging techniques and their appli-
cation to wavy flows. *Advances in Coastal and Ocean Engineering, 9*(1).

Tamburrino, A., and J. S.Gulliver, (2007), Free-surface visualization of streamwise vortices in a channel flow. *Water Resources Research, 43*(11).

Uijttewaal, W. S. J., and R. Booij (2000), Effects of shallowness on the development of free-surface mixing layers, *Phys. of Fluids (1994-present), 12*(2), 392-402.

Variano, E. A., and E. A. Cowen (2008), A random-jet-stirred turbulence tank. *Journal of Fluid Mechanics, 604*: 1-32.

Weitbrecht, V., G. Kuhn, G. H. Jirka (2002), Large scale PIV-measurements at the surface of shallow water flows. *Flow Measurement and Instrumentation, 13*: 237-245

Wereley, S. T., C. D. Meinhart, (2001), Second-order accurate particle image velocimetry. Experiments in Fluids, 31(3), 258-268.

Westerweel, J. (1994), Efficient detection of spurious vectors in particle image velocimetry data. *Exp. in Fluids, 16*: 236-247
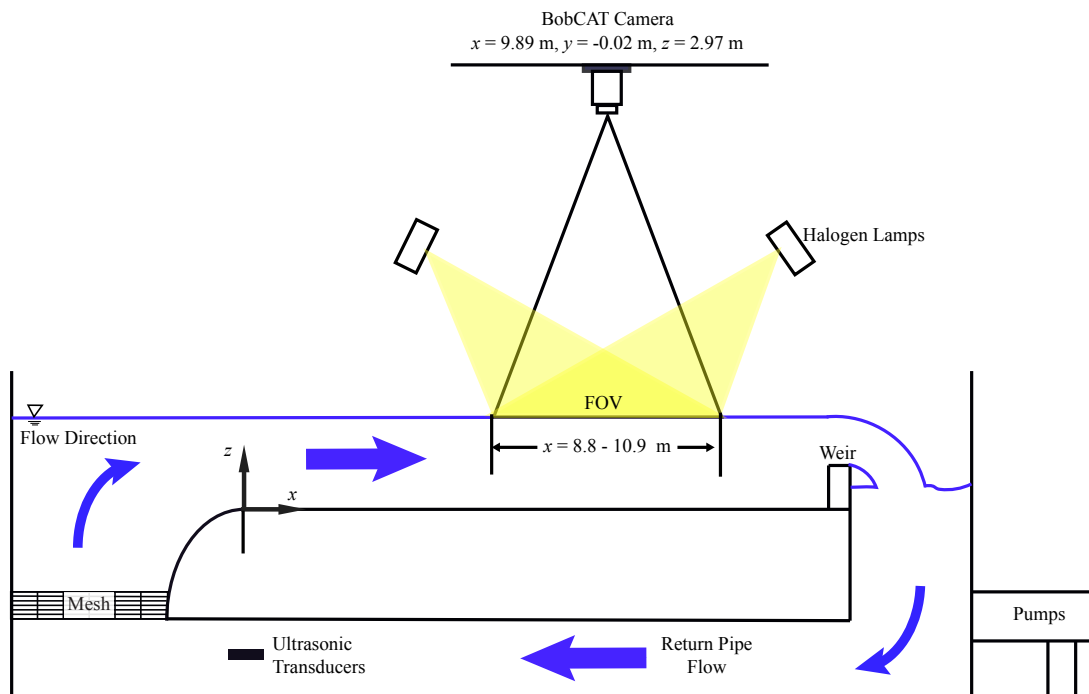
Figure 1. Schematic of recirculating wide-open channel flume.
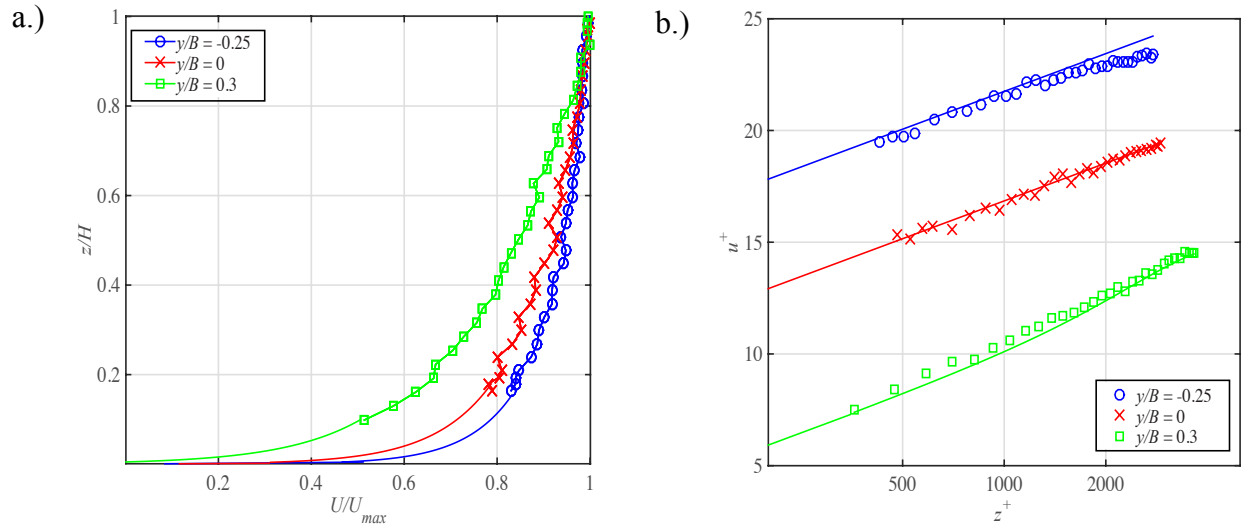
Figure 2.   Rough bed case, $H = 0.20$ m , $U_B = 0.22$ m/s a.) Normalized velocity profiles at $y/B =$ -0.25 (over glass bed) with $\delta^* = 20.9$ mm, $y/B = 0$ (channel centerline) with $\delta^* = 25$ mm, and y/B=0.3 (over rough bed) with $\delta^* = 47.8$ mm. Markers indicate measured points and smooth lines below $z/H < 0.2$ designate the log-law extrapolated results to the bed. b.) Vertical velocity profiles plotted in wall coordinates. Lines indicate log-wake fit.
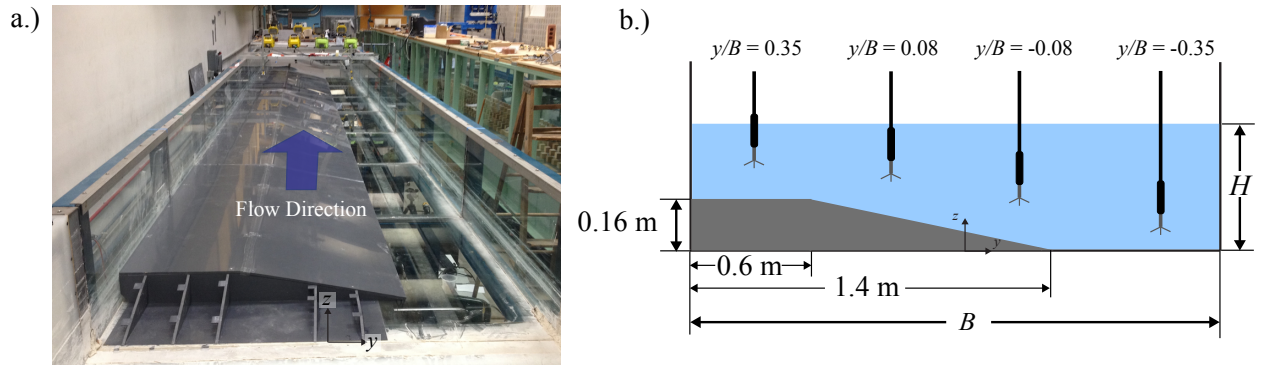
Figure 3. a.) Compound channel experimental set-up. Note: Front cover of the false-bottom insert has been removed to reveal the cross-section. b.) Compound channel schematic with ADV measurement positions indicated.
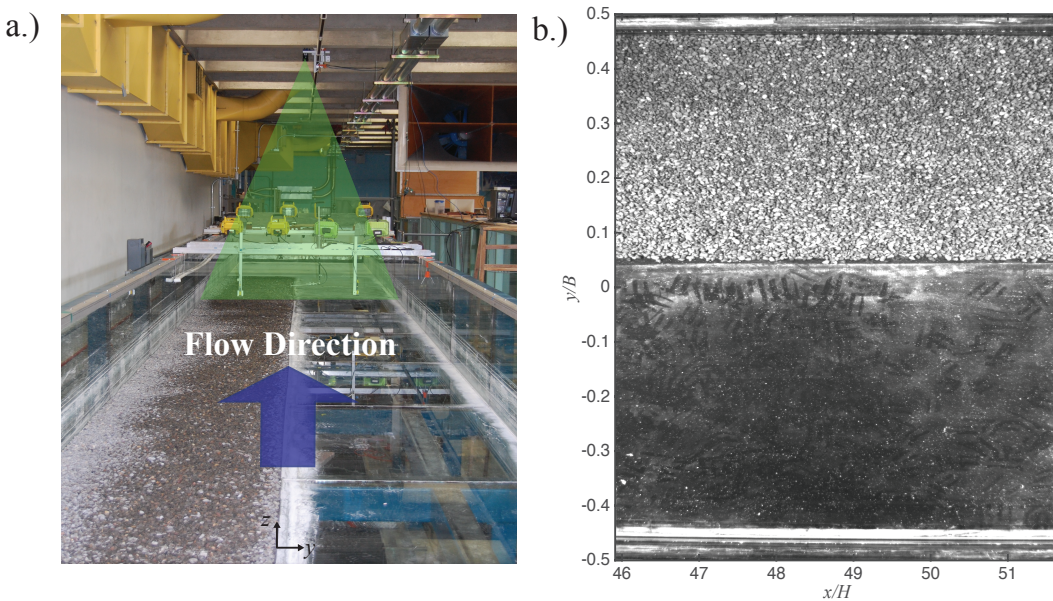
Figure 4. a.) Rough bed experimental set-up. b.) Rough bed camera field-of-view.
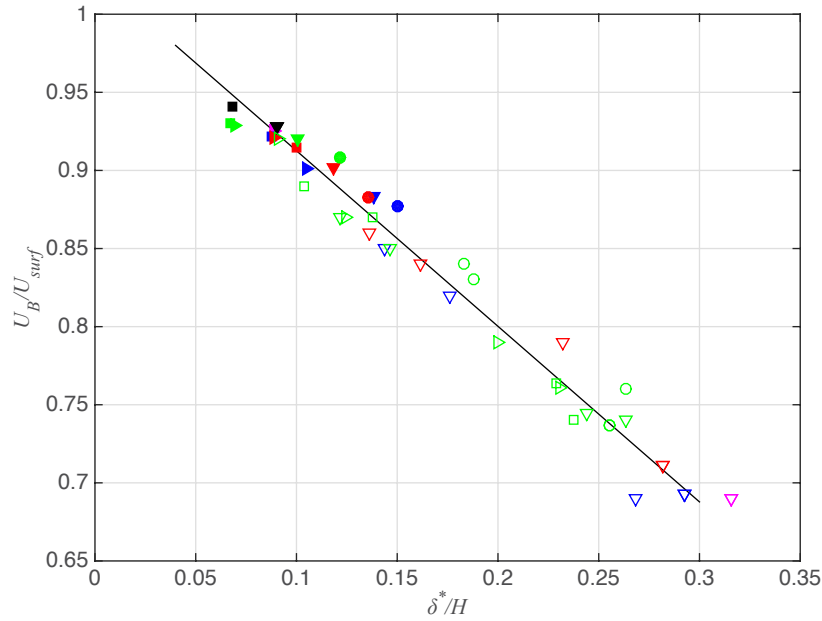
Figure 5.   Index velocity vs. displacement thickness normalized by the flow depth. Magenta

symbols, $H = 0.06 - 0.08$ m; Blue symbols, $H = 0.10 - 0.11$ m; Red symbols, $H = 0.15 - 0.16$

m; Green symbols, $H = 0.20 - 0.21$ m; Black symbols, $H = 0.31$ m. ○, $U_B = 0.05$ m/s; ▽,

$U_B = 0.09 - 0.1$ m/s; □, $U_B = 0.23 - 0.24$ m/s; ▷, $U_B = 0.33 - 0.35$ m/s. Filled-in symbols

indicate smooth bed cases and hollow symbols indicate rough bed cases.
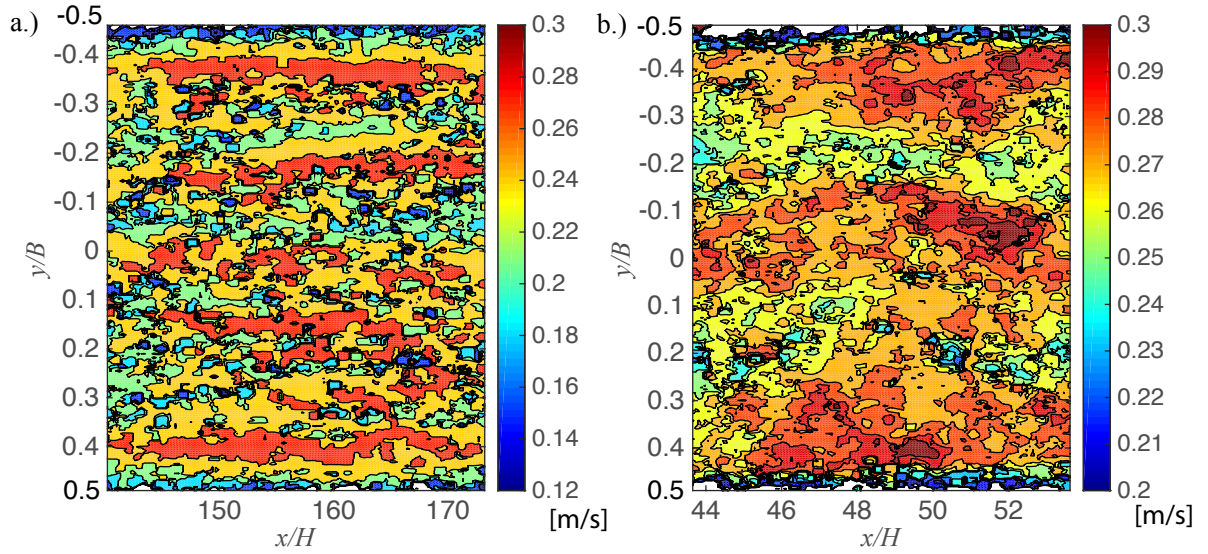
Figure 6. Instantaneous streamwise velocity contours. a.) Smooth bed experimental case H = 0.06 m, U_B = 0.23 m/s. b.) Smooth bed experimental case H = 0.20 m, U_B = 0.24 m/s.
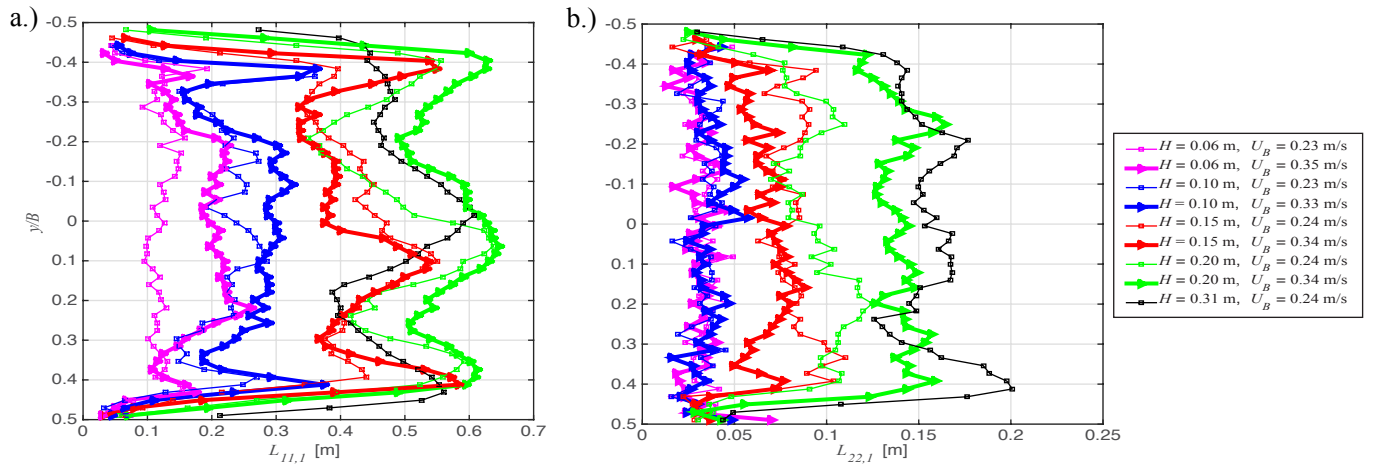
Figure 7. Smooth bed cases. a.) Streamwise integral length scale, $L_{11,1}$ vs. non-dimensional channel width. b.) Transverse integral length scale, $L_{22,1}$ vs. non-dimensional channel width.
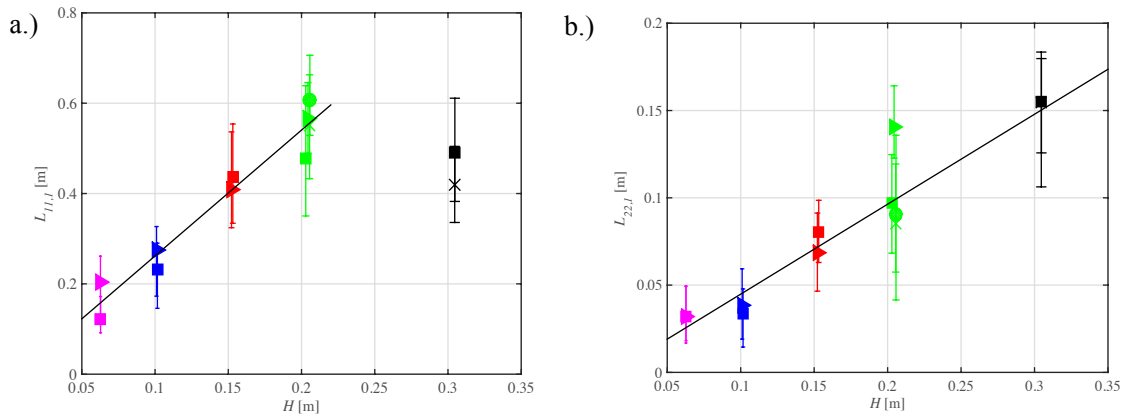
Figure 8.   Smooth bed cases. a.) Mean streamwise integral length scale plotted against flow depth. Solid line: $y = 2.79(x) - 0.02, R^2 = 0.95$. b.) Mean transverse integral length scale plotted against flow depth. Solid line: $y = 0.52(x) - 0.01, R^2 = 0.96$. Error bars indicate the range of values across the channel. See caption in Figure 5 for explanation of symbols.
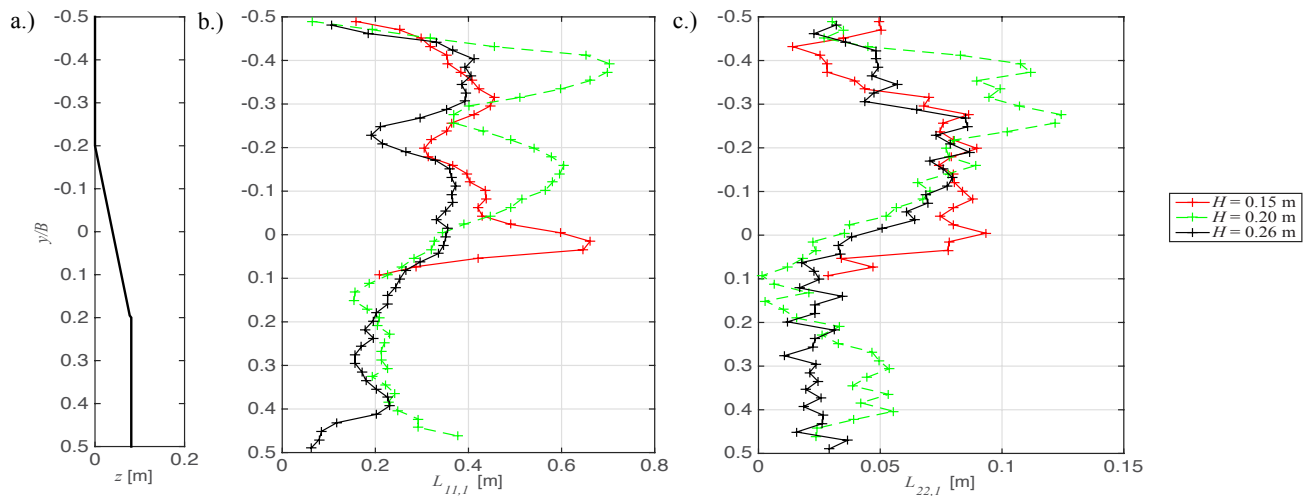

Figure 9.   Compound channel cases. a.) Compound channel cross section. b.) Streamwise integral length scale, $L_{11,1}$ vs. non-dimensional channel width. c.) Transverse integral length scale, $L_{22,1}$ vs. non-dimensional channel width.
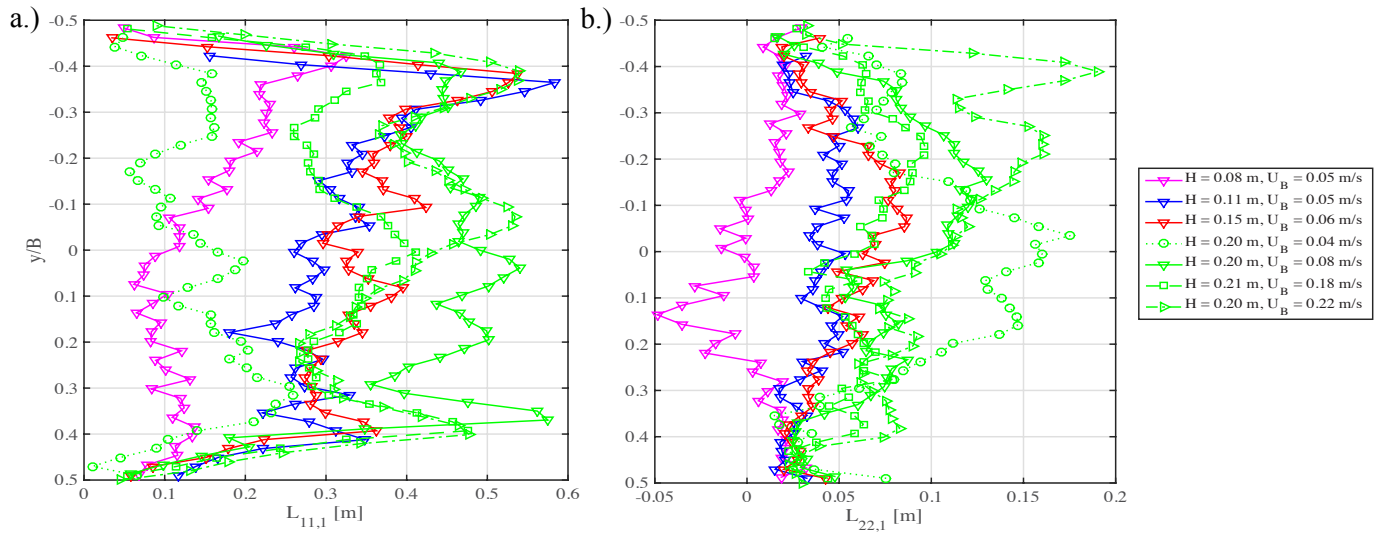
Figure 10. Rough bed cases. a.) Streamwise integral length scale, $L_{11,1}$ vs. non-dimensional channel width. b.) Transverse integral length scale, $L_{22,1}$ vs. non-dimensional channel width. U_B values reported in the legend correspond to depth-averaged velocities measured over the rough bed.
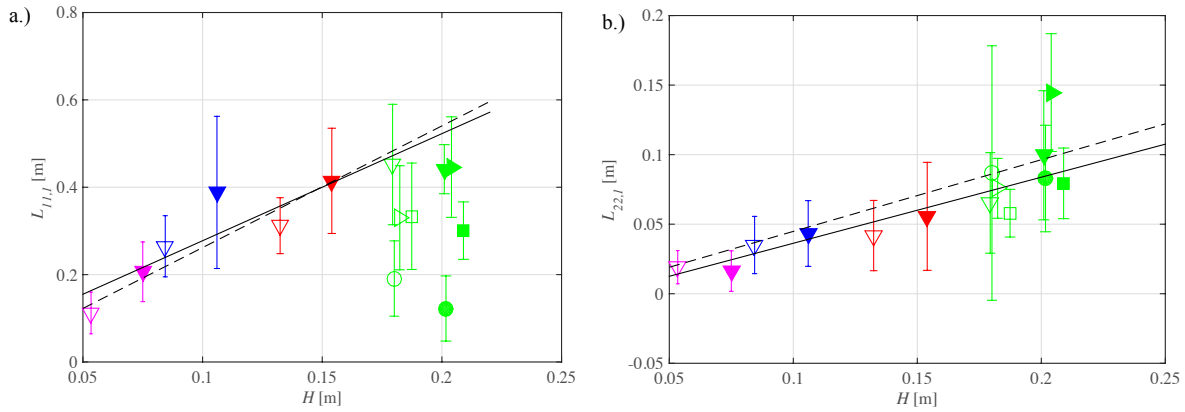
Figure 11.   Rough bed cases. a.) Mean streamwise integral length scale plotted against flow depth. Solid line, best fit for rough bed cases, $y = 2.45(x) + 0.03, R^2 = 0.83$. Dashed line, best fit for smooth bed cases, $y = 2.79(x) - 0.02$ (from Fig 8a). b.) Mean transverse integral length scale plotted against flow depth. Solid line, best fit for rough bed cases, $y = 0.47(x) - 0.01, R^2 = 0.90$. Dashed line, best fit for smooth bed cases, $y = 0.52(x) - 0.007$ (from Fig 8b). Error bars indicate the range of values across the channel. See caption in Figure 5 for explanation of symbols. Hollow symbols are data measured directly over the rough bed and filled symbols are data measured over the smooth bed side of the rough bed cases.
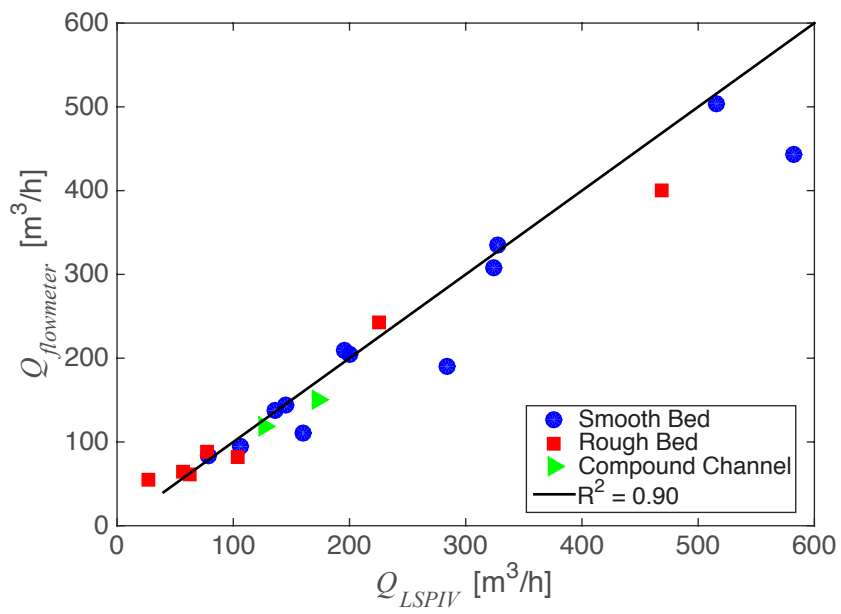
Figure 12. Measured vs. predicted volumetric discharge.

Table 1.   Smooth bed experimental flow cases.

H [m]	B/H	U_b [m/s]	Re_H[a]	Fr [b]	δ^*/H	u^*[c][mm/s]
0.06	31.8	0.23	14,606	0.33	0.13	14.0
0.06	31.9	0.35	21,795	0.46	0.09	18.0
0.11	19.1	0.05	4,948	0.05	0.15	3.0
0.11	18.7	0.09	9,574	0.10	0.13	6.1
0.10	19.7	0.23	23,396	0.25	0.09	11.8
0.10	19.8	0.33	32,895	0.36	0.10	18.0
0.16	12.8	0.05	7,023	0.04	0.13	2.80
0.15	13.1	0.10	14,543	0.08	0.11	6.0
0.15	13.1	0.24	35,835	0.20	0.10	12.0
0.15	13.1	0.34	50,935	0.29	0.09	16.0
0.21	9.7	0.05	10,654	0.04	0.12	3.0
0.21	9.7	0.10	19,649	0.07	0.10	5.2
0.20	9.9	0.24	48,704	0.18	0.07	12.0
0.20	9.8	0.34	70,033	0.26	0.07	16.5
0.31	6.6	0.10	29,095	0.06	0.09	5.5
0.31	6.6	0.24	73,747	0.14	0.07	11.0

[a] Re_H is the Reynolds number formed with the depth-averaged velocity and flow depth.

[b] Fr is the Froude number formed with the centerline velocity and flow depth.

[c] u^* is the friction velocity.

Table 2.   Compound channel experimental flow cases.

H [m]	U_b[a][m/s]	D_r	δ^* [mm]	u^*[a][mm/s]
0.15	$0.21 - 0.22$	0	$13 - 17$	11.0
0.20	$0.20 - 0.23$	0.19	$13 - 20$	$9.9 - 11.0$
0.26	$0.18 - 0.24$	0.37	$128 - 190$	$9.3 - 11.2$

[a] The range of values for U_B and u^* reflect multiple measurements taken at the multiple

locations discussed in Section 2.4.

Table 3.   Rough bed experimental flow cases.

H [m]	B/H	U_b[a][m/s]	Re_H	Fr	δ^*/H	k_{rms}	u^*[a][mm/s]
0.08	26.7	0.05 - 0.14	4,893	0.11	0.32	0.29	15.5 - 17.0
0.11	18.9	0.05 - 0.10	6,018	0.08	0.29	0.20	7.0 - 8.2
0.15	13	0.06 - 0.08	10,430	0.08	0.28	0.14	4.8 - 5.4
0.20	9.9	0.04 - 0.04	7,735	0.04	0.26	0.11	3.2 - 3.4
0.20	10	0.08 - 0.11	13,674	0.06	0.24	0.11	5.6 - 8.0
0.21	9.6	0.18 - 0.26	36,804	0.16	0.23	0.10	13.5 - 17.5
0.20	9.8	0.22 - 0.28	51,671	0.24	0.23	0.11	13.0 - 19.0

[a] The range of values for U_B and u^* reflect multiple measurements taken at the multiple

locations discussed in Section 2.4.